Article

$M_xLa_{1-x}SiO_{2-y}N_z$ (M = Ca/Sr/Ba): Elucidating and Tuning the Structure and Eu²⁺ Local Environments to Develop Full-Visible Spectrum Phosphors

Mahdi Amachraa, Shuxing Li, Po-Yuan Huang, Ru-Shi Liu, Zhenbin Wang,* Rong-Jun Xie,* and Shyue Ping Ong*

Cite This: https://doi.org/10.1021/acs.chemmater.2c00252

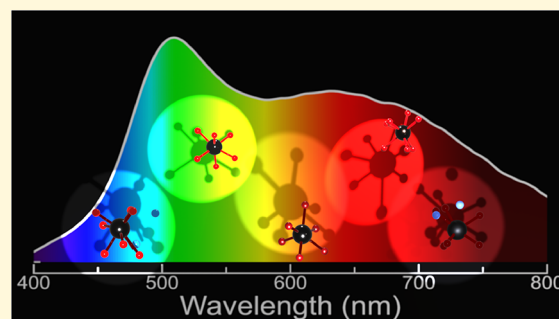Read Online

ACCESS | 📊 Metrics & More | 📖 Article Recommendations | 🆂🅸 Supporting Information

ABSTRACT: The local environments of rare-earth activators have profound effects on the luminescent properties of phosphors. Here, we elucidate the crystal structure of the $LaSiO_2N$ phosphor host using a combination of density functional theory calculations and synchrotron X-ray diffraction. We determine that $LaSiO_2N$ crystallizes in the monoclinic $C2/c$ instead of the hexagonal $P\bar{6}c2$ space group. To improve the luminescence performance, divalent cations M (M = Ca/Sr/Ba) were introduced into $LaSiO_2N$ to eliminate Eu³⁺. A family of apatite $M_{1+x}La_{4-x}Si_3O_{13-x/2}$:Eu²⁺ ($x \sim 1.5$, M = Ca/Sr/Ba) phosphors was further developed with unprecedented ultra-broadband (290 nm) emission spectra and excellent thermal stability. Detailed local environment investigations reveal that the formation of oxygen vacancies within and beyond the first-shell environment of Eu²⁺ is responsible for the redshift and broadening of the emission spectra *via* geometrical alteration of the Eu²⁺ local environment. This work provides new insights for understanding and optimizing the luminescence of rare-earth phosphors.

■ INTRODUCTION

The luminescent properties of rare-earth-activated phosphors are heavily influenced by the chemical and structural properties of the host lattice.[1] For the Eu²⁺ activator operating on the $4f^65d^1 \rightarrow 4f^7$ transition, previous studies[2,3] have attributed the total redshift (D) of the 5d energy levels to two additive and independent interactions: the centroid shift (ϵ_c) and the crystal field splitting (ϵ_{cfs}). Broadly, the *in-crystal* anion polarizability/covalency controls the 5d centroid shift, while the size and shape of the Eu²⁺−ligand polyhedron dictate the crystal-field splitting of Eu²⁺ 5d orbitals. Therefore, accurate information of the host structural lattice, electronic properties, and the activator's local environment is critical to understanding and tuning the luminescent behaviors of phosphors.[4] However, such information is particularly challenging to obtain for polyanionic ligands or lattices with large compositional network flexibility and typically requires a combination of advanced experimental characterization techniques and theoretical calculations.[5] The M/La−Si−O−N (M = Ca/Sr/Ba) chemical space is of high interest in phosphor materials.[6,7] In particular, to investigate the impact of the Eu and M−La−Si−O−N interactions, the $LaSiO_2N$ phase represents a good starting point as it provides a compositional pathway to several La−Si−O−N phases, as shown in the experimental phase diagram[8] (see Figure S1).

In 1977, Wills and Cunningham discovered a new group of silicon lanthanide (Ln) oxynitrides by reacting Si_3N_4 with

several lanthanide oxides, where the X-ray diffraction (XRD) patterns of $LaSiO_2N$ were first reported.[9] Shortly after, Morgan and Carroll proposed that $LaSiO_2N$ has a pseudo-hexagonal lattice with the $P\bar{6}c2$ space group and lattice parameters a = 7.31 Å and c = 9.55 Å.[10] Later, however, Mitomo *et al.* reported that $LaSiO_2N$ forms a monoclinic $C2/c$ or Cc (a = 12.695 Å, b = 7.327 Å, c = 28.557 Å, and β = 90.81°) and is analogous to the pseudo-wollastonite structure of $SrGeO_3$ with a repeat distance, c, that is nearly three times larger than the one suggested by Morgan.[8] Furthermore, starting from the wollastonite phase ($LaSiO_2N$), the formal exchange of nitrogen by oxygen leads to several compounds, such as $La_4Si_2O_7N_2$, $La_5Si_3O_{12}N$, $La_{4.67}Si_3O_{12}$, and $La_2Si_6N_8O_3$. Morgan noted that a solid solution $Ln_{1-x}^{3+}Ln_x^{4+}SiO_{2-x}N_{1+x}$, may occur as long as the local charge balance (Pauling's second rule) is preserved.[9] It is our hypothesis that some alkaline-earth ion M^{2+} (M = Ca/Sr/Ba) can be introduced into $LaSiO_2N$ to form solid solutions of $Ln_{1-x}^{3+}M_x^{2+}SiO_{2+y}N_{1-z}$ and provide alternative Eu²⁺−host interactions to optimize the luminescence of $LaSiO_2N$:Eu.
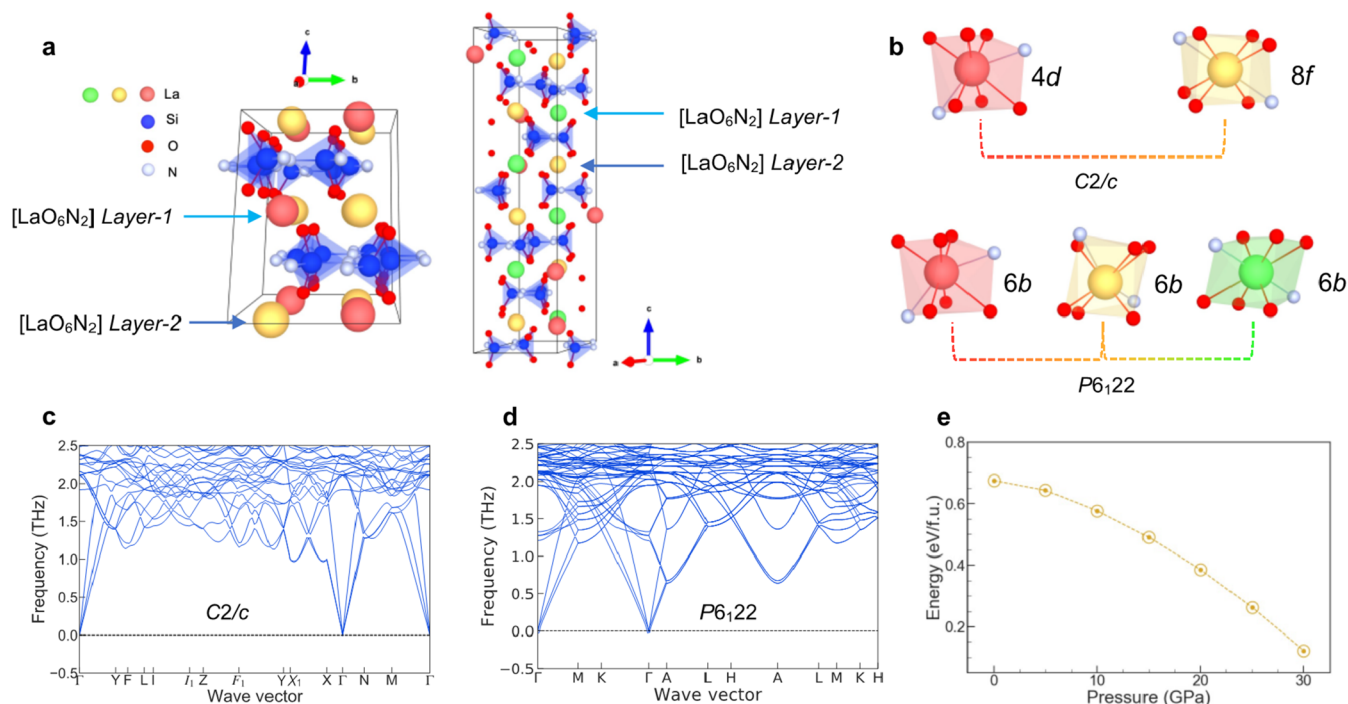
A

Figure 1. Computational determination of the LaSiO$_2$N crystal structure. The crystal structures of LaSiO$_2$N under (a) $C2/c$ and $P6_122$ space groups. (b,c) [LaO$_6$N$_2$] polyhedron in LaSiO$_2$N $C2/c$ (two non-equivalent sites labeled with Wyckoff symbols 4d and 8f) and $P6_122$ (three non-equivalent sites labeled with Wyckoff symbol 6b) phases, respectively. (c,d) DFT-computed phonon spectra for the $C2/c$ and $P6_122$ phases of LaSiO$_2$N. (e) Calculated enthalpy barrier of phase transformation from the $C2/c$ to the $P6_122$ phase as a function of hydrostatic pressure.

In this work, we first determined the LaSiO$_2$N crystal structure by combining crystal structure predictions based on density functional theory (DFT) calculations with synchrotron X-ray diffraction (SXRD) measurements. Our results indicate that LaSiO$_2$N crystallizes into the monoclinic $C2/c$ instead of the $P\bar{6}c2$ space group. To eliminate the Eu^{3+} in LaSiO$_2$N, mixed divalent M cations (M = Ca/Sr/Ba) were introduced into the LaSiO$_2$N lattice, with the concomitant replacement of N^{3-} with O^{2-} to maintain charge balance. The oxygen-rich end-member M_{1+x}La$_{4-x}$Si$_3$O$_{13-x/2}$:Eu^{2+} ($x \sim 1.5$, M = Ca/Sr/Ba) phosphors show a broad green/red emission, significantly improved quantum efficiency (QE), and excellent thermal stability. We further uncovered that the formation of oxygen vacancies (V$_O^{\bullet\bullet}$) within the first-shell environment of Eu$_{Sr/Ca}$ and beyond the first-shell environment of Eu$_{Ba}$ is responsible for the enhanced luminescence performance. Finally, a prototype phosphor-converted white-light-emitting diode (LED) was constructed by mixing the developed Ba-type apatite with the commercial blue phosphor BaMgAl$_{10}$O$_{17}$:Eu^{2+} and yields an excellent white-light-color-rendering index (CRI = 93) with chromaticity coordinates located at (0.32, 0.33) and a correlated color temperature (CCT) of 6080 K.

■ RESULTS AND DISCUSSION

Computational Structure Prediction. Candidate phases in the La−Si−O−N chemical space were generated using the data-mined ionic substitution algorithm of Hautier et al.[11] Following DFT relaxation and energy calculations (see Materials and Methods for details), two thermodynamically stable and symmetrically distinct phases of LaSiO$_2$N were uncovered: the monoclinic $C2/c$ (15) and hexagonal $P6_122$ (178), as shown in Figure 1a. The parent structures of monoclinic $C2/c$ and hexagonal $P6_122$ are NaBOF$_2$ (ICSD no.

424505)[12] and YSiO$_2$N (ICSD no. 151752),[12] respectively. In the monoclinic $C2/c$ lattice, La occupies two distinct crystallographic sites (Figure 1b), with Wyckoff symbols 8f and 4d. On the other hand, the $P6_122$ phase shows three distinct crystallographic sites with Wyckoff symbol 6b (Figure 1b). Each La site forms a distorted cubic local environment composed of six O^{2-} and two N^{3-} ligands. The calculated lattice parameters and atomic coordinates are provided in Tables 1 and 2, respectively. As shown in Table 1, the lattice

Table 1. Theoretically Calculated Lattice Constants and Phase Stability (E_{hull}, eV/Atom) of the Predicted $C2/c$ and $P6_122$ and Experimental Phases of LaSiO$_2$N^a

phase	$P\bar{6}c2$	$P6_122$	$C2/c$	$C2/c$ or Cc
a (Å)	7.310	7.270	12.578	12.695
b (Å)	7.310	7.270	7.287	7.327
c (Å)	9.550	28.500	10.340	28.557
α (deg)	90	90	90	90
β (deg)	90	90	113.33	90.81
λ (deg)	120	120	90	90
E_{hull}	1.05	0	0	
refs	10	this work	this work	8

^{a}The lattice constants of the phase $C2/c$ or Cc obtained from refs 8 and 10 are experimental values.

parameters of our predicted monoclinic $C2/c$ (15) phase are equivalent to those determined by Mitomo et al.[8] except for the c lattice constant and β angle. Table 1 also presents the calculated relative phase stability, characterized by the computed energy above hull (E_{hull}), of the two predicted phases and the previously reported hexagonal $P\bar{6}c2$ (188).[10] It should be noted that Mitomo et al.[8] determined the lattice

Table 2. Crystal Structure of LaSiO$_2$N C2/c Phase[a]

(a) Lattice Constants		
	Rietveld refinement	calculated
space group	C2/c	C2/c
a (Å)	12.6513(2)	12.57824
b (Å)	7.3305(1)	7.28701
c (Å)	10.3666(2)	10.33947
β (deg)	113.388(9)	113.3337
V (Å^3)	882.4112(2)	870.184020
R$_{wp}$	8.82%	
R$_p$	6.17%	
χ^2	2.63	

(b) Atomic Positions in C2/c									
	calculated			experimental					
site	x	y	z	x	y	z	Occ.	Wyckoff position	B$_{eq}$ (Å^2)
La1	0.08768	0.23821	0.99870	0.0873(3)	0.239(3)	0.998(4)	1	8f	0.0647(6)
La2	0.25000	0.25000	0.50000	0.25	0.25	0.5	1	4d	0.0123(1)
Si3	0.11893	0.46232	0.74589	0.117(9)	0.465(2)	0.744(1)	1	8f	0.0532(2)
Si4	0.00000	0.17973	0.25000	0	0.181(2)	0.25	1	4e	0.344(4)
N5	0.11381	0.30349	0.24635	0.111(2)	0.311(4)	0.251	1	8f	0.0625(6)
N6	0.00000	0.35315	0.75000	0	0.338(6)	0.75	1	4e	0.839(1)
O7	0.05140	0.06353	0.39999	0.0450(2)	0.071(3)	0.389(2)	1	8f	0.0242(6)
O8	0.12681	0.40352	0.59538	0.140(2)	0.403(3)	0.605(2)	1	8f	0.0227(6)
O9	0.22637	0.40565	0.89689	0.226(2)	0.404(3)	0.902(2)	1	8f	0.0144(6)

[a](a) Theoretically calculated lattice parameters and Rietveld refinement parameters of SXRD patterns of the C2/c phase of LaSiO$_2$N. (b) Theoretically calculated and SXRD-refined atomic coordinates, occupancy, and atomic displacement parameter (B$_{eq}$) for LaSiO$_2$N (C2/c).
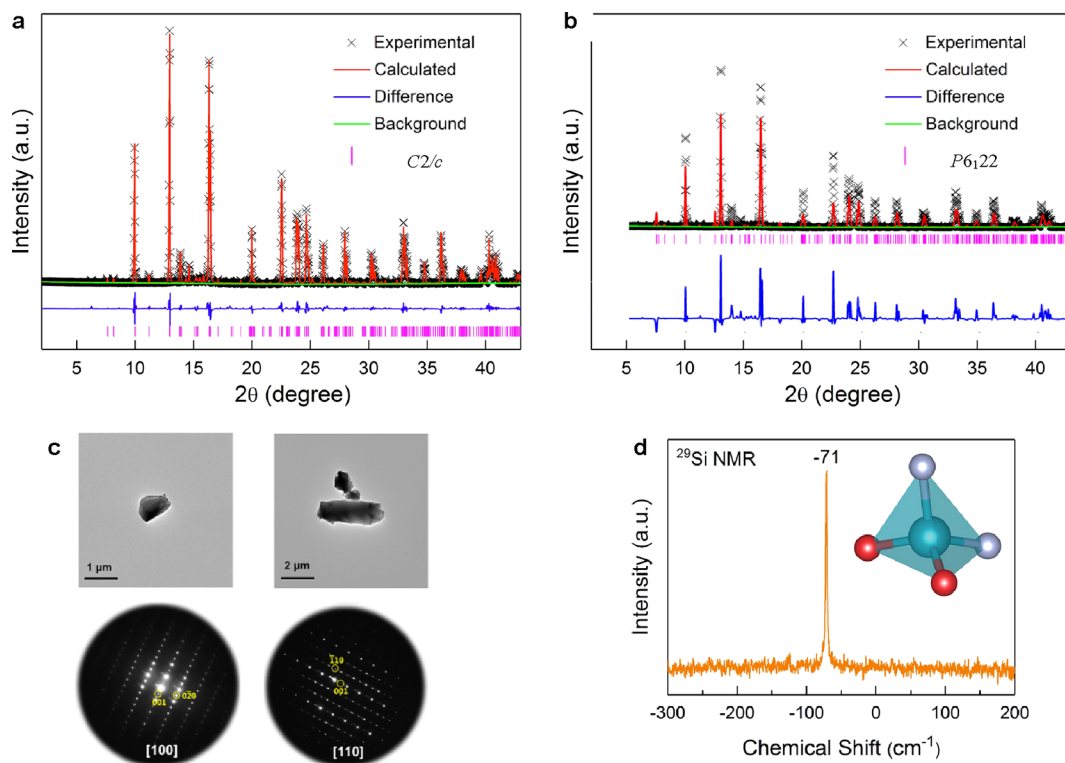

Figure 2. Experimental determination of the LaSiO$_2$N crystal structure. (a) SXRD of the Rietveld refinement of LaSiO$_2$N with the initial model in the space group of C2/c (R$_{wp}$ = 8.82%, R$_p$ = 6.17%, χ^2 = 2.63). (b) SXRD of the Rietveld refinement of LaSiO$_2$N with the initial model in the space group of P6$_1$22 (R$_{wp}$ = 47.76%, %, χ^2 = 14). (c) Transmission electron microscopy (TEM) images and SAED patterns along [100] and [110] zone axes, respectively. (d) ^{29}Si NMR spectrum indicates the local coordination environment of SiO$_2$N$_2$, as shown in the inset (the cyan sphere refers to Si atoms; red spheres refer to O atoms; and light gray spheres refer to N atoms).

parameters based on electron diffraction patterns and did not report the atomic coordinates for their monoclinic phase, and

we, therefore, could not perform DFT calculations for that structure for comparison.
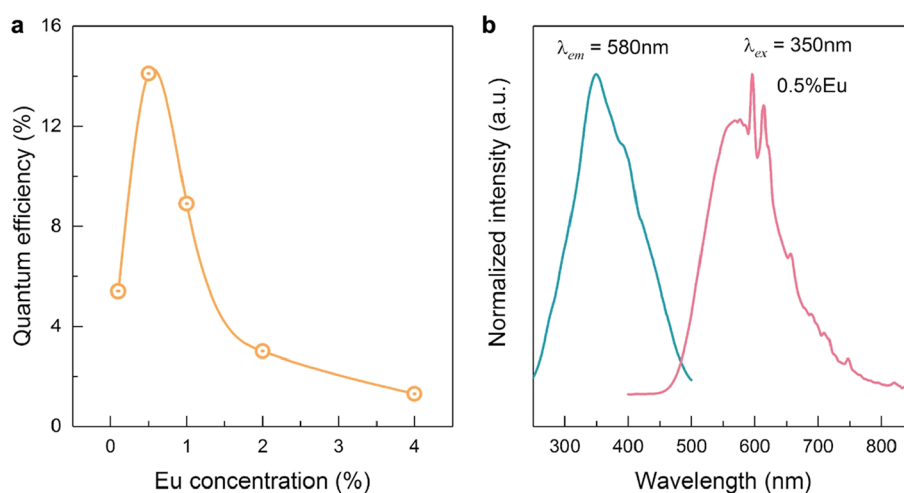
Figure 3. PL LaSiO$_2$N:Eu ($C2/c$). (a) IQE as a function of the Eu concentration (0.1−4%) and (b) normalized excitation and emission spectra of LaSiO$_2$N:0.5%Eu.
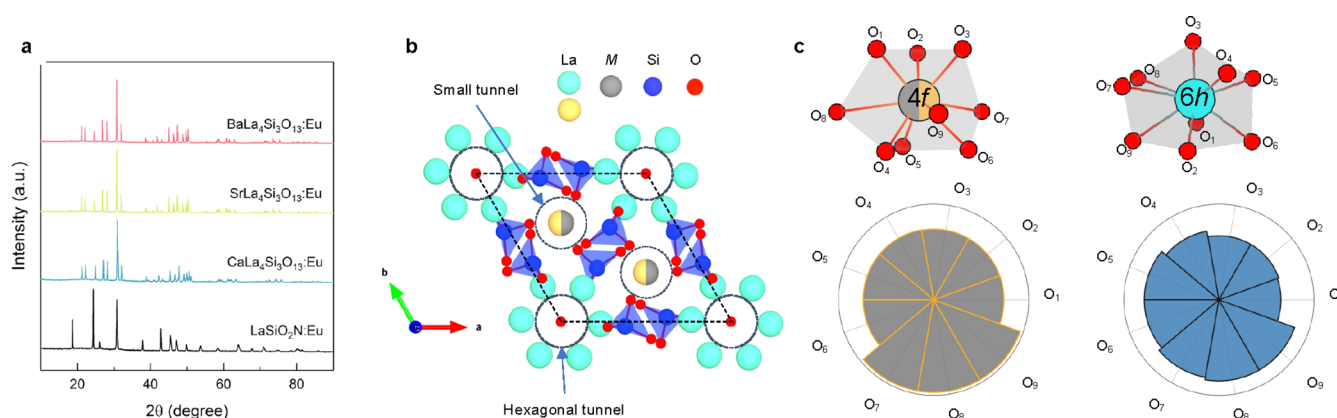

Figure 4. Crystal structure evolution of LaSiO$_2$N upon M cation insertion. (a) Conventional XRD patterns of LaSiO$_2$N:0.5%Eu, CaLa$_4$Si$_3$O$_{13}$:0.5%Eu, SrLa$_4$Si$_3$O$_{13}$:0.5%Eu, and BaLa$_4$Si$_3$O$_{13}$:0.5%Eu. (b) Crystal structure of the apatite MLa$_4$Si$_3$O$_{13}$ (M = Ca/Sr/Ba) and the formed hexagonal tunnel. (c) Cationic local environments of M/La at the 4h and 6h Wyckoff positions in MLa$_4$Si$_3$O$_{13}$ and a radar chart comparison of the local environment bond lengths.

The E_{hull} is a measure of the stability of a compound with respect to the stable phases in the DFT-calculated 0 K phase diagram. A stable phase has an E_{hull} of 0 eV/atom, and the higher the E_{hull}, the more unstable the phase is predicted to be. It is observed from Table 1 that both predicted monoclinic $C2/c$ and hexagonal $P6_122$ phases are more thermodynamic than the experimentally reported hexagonal $P\bar{6}c2$ phase[10] by 1.05 eV/atom. We also notice that the difference in the calculated formation enthalpies (Figure S2) between the two predicted phases ($C2/c$ and $P6_122$) is trivial (≤0.005 eV/f.u.). The relative thermodynamic stability of the two polymorphs is unchanged by temperature or pressure (Figure S2). These results are in line with the previous finding that wollastonite polytypes are insensitive to pressure−temperature changes.[13] Phonon spectrum calculations further indicate that both the predicted monoclinic $C2/c$ and hexagonal $P6_122$ are dynamically stable (Figure 1c,d). Additionally, we applied the variable cell nudged elastic band (VC-NEB) method[14] to investigate whether a kinetic barrier (solid-state transformation) exists along a $C2/c-P6_122$ transition pathway. Figure 1e shows the calculated kinetic barrier of the monoclinic $C2/c$ to the hexagonal $P6_122$ phase transition with respect to the pressure. We observe that this kinetic barrier significantly

decreases with increasing pressure, suggesting that the hexagonal $P6_122$ phase is likely to be accessed under high-pressure conditions.

Experimental Structure Determination. Samples of LaSiO$_2$N powder were synthesized at 1600−1700 °C under 0.9 MPa N$_2$ pressure. A comparison between the conventional XRD patterns of the two predicted phases ($C2/c$ and $P6_122$) and the two experimentally reported phases [$C2/c$ or Cc PDF#36-0572; $P\bar{6}c2$ (188), PDF#31-0669] shows minor differences among these patterns, which may explain the historical disagreements of previous structure determination (Figure S3).[8,10] The SXRD patterns were collected at room temperature and refined against the predicted crystal structures of the monoclinic $C2/c$ and hexagonal $P6_122$. Refinements against the monoclinic $C2/c$ show residual factors of R_{wp} = 8.82% and R_p = 6.17% (Figure 2 and Table 2) and lead to similar lattice constants to the computed ones, confirming our computational structure predictions. The refinement of the SXRD data with the hexagonal $P6_122$ phase was unsuccessful as reflected by the high-weighted percent R-factor (R_{wp} = 47.76%) (Figure 2b). The experimentally refined bond lengths of the LaO$_6$N$_2$ polyhedrons are listed in Table S3. The average bond La$_{4d}$−O/N and La$_{8f}$−O/N bond lengths are 2.62417(4)

Figure 5. PL evolution from $LaSiO_2N$:Eu to $M_{1+x}La_{4-x}Si_3O_{13-x/2}$:Eu. (a–c) Measured PL spectra of $LaSiO_2N$:Eu, $MLa_4Si_3O_{13}$:Eu, and $M_{1+x}La_{4-x}Si_3O_{13-x/2}$:Eu ($M$ = Ca/Sr and Ba; $x \sim 0$ and 1.5). (d) Comparison of emission spectra between $BaLa_4Si_3O_{13}$:Eu and $Ba_{1+x}La_{4-x}Si_3O_{13-x/2}$:Eu ($x \sim 1.5$) and the Gaussian deconvolution of the $Ba_{1+x}La_{4-x}Si_3O_{13-x/2}$:Eu emission spectrum into two peaks from two distinct sites: Eu_{4h} and Eu_{6h}. (e) Evolutions of the M/La cation site occupancy upon La substitution by M (M = Ca/Sr/Ba): (i) $LaSiO_2N$; (ii) $MLa_4Si_3O_{13}$; and (iii) $M_{1+x}La_{4-x}Si_3O_{13-x/2}$ (unconstructed).

and 2.57568(4) Å, respectively. The space group of the polycrystal was further confirmed through selected area electron diffraction (SAED), as shown in Figure 2c. The sizes of the well-crystallized particles are around 1 to 5 μm. The SAED patterns observed from the directions of [100] and [110] zone axes were accurately indexed against the monoclinic $C2/c$ space group. The ^{29}Si nuclear magnetic resonance (NMR) spectrum shows a sharp signal at −71 ppm assigned to $[SiO_2N_2]$ (Figure 2d). This NMR result shows that $LaSiO_2N$ is built up with the $[SiO_2N_2]$ tetrahedra, forming a three-dimensional network structure instead of the clustered N atoms found in the previously reported $P\bar{6}c2$ phase (Figure S4).[10]

Chemical Site Engineering through Mixed-Cation Solid Solutions. The photoluminescence (PL) behavior of $LaSiO_2N$:Eu was optimized as a function of the Eu concentration as shown in Figure 3a. An Eu concentration of 0.5% leads to an optimal excitation and emission peaking at 350 and 580 nm, respectively (Figure 3b). The measured internal QE (IQE) and absorption efficiencies are 14 and 50%, respectively. The relatively low IQE is predominantly attributed to Eu^{3+}, as manifested by the characteristic sharp lines at around 610 nm in the emission spectrum. To eliminate the adverse effect of Eu^{3+}, alkaline-earth metals M (such as M = Ca/Sr/Ba) were introduced into $LaSiO_2N$. The substitution of

La−N with M−O shifts the composition toward the oxygen-rich region of the $La_2O_3−SiO_2−Si_3N_4$ phase diagram (Figure S1) and results in the stabilization of the apatite-like $MLa_4Si_3O_{13}$ phase ($P6_3/m$, M = Ca/Sr/Ba) (Figure 4a and Table S3). The $MLa_4Si_3O_{13}$ crystal structure comprises isolated $[SiO_4]^{4-}$ complexes (Figure 4b). The spatial formation of these complexes leads to the formation of two cationic sites with distinct Wyckoff positions, namely, 4f and 6h, as shown in Figure 4b, where the M_{4h} cations build up chains of face-sharing polyhedra that are interconnected via the SiO_4 groups, and the M_{6h} cations form a sixfold hexagonal channel around interstitial oxygen (Figure 4b). The crystal structures of the $MLa_4Si_3O_{13}$ show that M/La partially occupies the 4f-site and is coordinated with nine oxygens (six near ones forming Hoppe's effective[15] trigonal prism coordination environment and three distant ones forming a tricapped triangular prism), and the 6h-site is fully occupied by La and is coordinated with nine oxygens forming highly distorted Hoppe's effective octahedron (Figure 4c). Furthermore, as shown in Figure S5, oxygen anions occupy four symmetrically inequivalent Wyckoff positions (2a, 6h, 6h, and 12i), whereas the anions located at the 2a positions represent the hexagonal channel-free oxygen ion. The introduction of additional M cations will lead to the substitution of La_2O_3 by MO and can be represented as follows
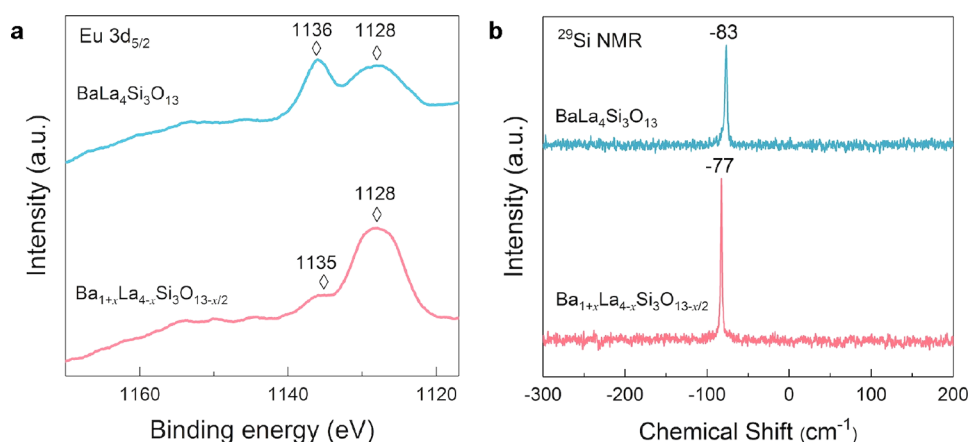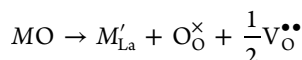
Figure 6. Experimental investigation of defect centers. (a) High-resolution XPS spectra of the Eu 3d region in $BaLa_4Si_3O_{13}$:Eu and $Ba_{1+x}La_{4-x}Si_3O_{13-x/2}$ ($x \sim 1.5$). (b) ^{29}Si NMR spectra of $BaLa_4Si_3O_{13}$:Eu and $Ba_{1+x}La_{4-x}Si_3O_{13-x/2}$ ($x \sim 1.5$).

Table 3. Theoretically Calculated Defect Formation Energies Eu^{2+} and Eu^{3+} (ΔE_f^d) in eV/Defect of Each Defect Configuration in $LaSiO_2N$ ($C2/c$) and $M_{1+x}La_{4-x}Si_3O_{13-x/2}$ ($P6_3/m$) (M = Ca/Sr/Ba)

compositions	$\Delta E_f^d[Eu_{La}]$ (Wy) (eV/Eu^{3+})		$\Delta E_f^d[Eu_M]$ (Wy) (eV/Eu^{2+})		$\Delta E_f^d[Eu_{La}] - \Delta E_f^d[Eu_M]$	
	site 1	site 2	site 1	site 2	site 1	site 2
$LaSiO_2N$	1.91 (4d)	2.12 (8f)				
$CaLa_4Si_3O_{13}$	2.24 (4f)	2.24 (6h)	0.06 (4f)	2.18	2.18	
$Ca_{1+x}La_{4-x}Si_3O_{13-x/2}$		1.97 (6h)	0.29 (4f)	0.02 (6h)	1.68	1.95
$SrLa_4Si_3O_{13}$	2.35 (4f)	2.43 (6h)	0.10 (4f)	2.25	2.33	
$Sr_{1+x}La_{4-x}Si_3O_{13-x/2}$		2.03 (6h)	0.06 (6h)	−0.13 (6h)	1.97	2.16
$BaLa_4Si_3O_{13}$	2.90 (4f)	3.26 (6h)	−0.213 (4f)	3.11	3.47	
$Ba_{1+x}La_{4-x}Si_3O_{13-x/2}$		1.92 (6h)	−0.50 (4f)	−0.71 (4f)	2.42	2.63

$$MO \rightarrow M'_{La} + O_O^\times + \frac{1}{2}V_O^{\bullet\bullet}$$

This substitution suggests that the apatite structure benefits from a large compositional flexibility, facilitating the aliovalent substitution of additional M^{2+} cations on the La^{3+} site ($M_{1+x}La_{4-x}Si_3O_{13-x/2}$) while simultaneously inducing oxygen vacancies and reducing the Eu^{3+}-compatible sites (La^{3+} sites). At the nominal composition of $M_{1+x}La_{4-x}Si_3O_{13-x/2}$ ($x = 1.5$), the XRD patterns and elemental analysis confirm the targeted composition (Figure S6a−c and Table S4). Beyond a concentration of $x = 1.5$, the apatite structure was found unstable because of the reduced content of O_{2a}-free anions.

Mixed-Cation-Induced Spectral Evolution. The emission spectra of $MLa_4Si_3O_{13}$:Eu ($x = 0$ in $M_{1+x}La_{4-x}Si_3O_{13-x/2}$) (Figure 5a−c) exhibit a much lower intensity of the Eu^{3+} characteristic peak compared to those of $LaSiO_2N$:Eu, confirming the stabilization of Eu^{2+} in the $MLa_4Si_3O_{13}$ compositions. The emission wavelengths (λ_{em}) for M = Ba, Sr, and Ca in $MLa_4Si_3O_{13}$:Eu are 503, 510, and 517 nm, respectively (Table 4). As shown in Figure 5a−c, the PL of $M_{1+x}La_{4-x}Si_3O_{13-x/2}$:Eu ($x \sim 1.5$) is compatible with the UV LED chip, showing excitation spectra peaking at 300−400 nm and ultra-broadband emission spectra of a 290 nm bandwidth. Interestingly, the emission spectra of $Sr_{1+x}La_{4-x}Si_3O_{13-x/2}$:Eu and $Ba_{1+x}La_{4-x}Si_3O_{13-x/2}$:Eu ($x \sim 1.5$) show red-shifted dual emission bands with maxima at 536/624 and 510/635 nm, respectively (Figure 5b,c), while $Ca_{1+x}La_{4-x}Si_3O_{13-x/2}$:Eu shows a single emission peak at 546 nm (Figure 5a). The dual-band character of these apatites is further confirmed through Gaussian deconvolution of the $Ba_{1+x}La_{4-x}Si_3O_{13-x/2}$:Eu ($x \sim 1.5$) emission spectrum, shown

in Figure 5d. The calculated occupancy at $x \sim 1.5$ from XRD Rietveld refinements indicates that the 4f positions are occupied by M cations, while the 6h positions have an M/La mixed occupancy explaining the substantial decrease in Eu^{3+} characteristic emission at $x \sim 1.5$.

Experimental Structural and Chemical Analysis of PL Behaviors. The results of scanning transmission electron microscopy (STEM) high-angle annular dark-field, cathodoluminescence (CL), and EDS analysis (Figure S7) reveal homogeneous elemental distributions and uniform luminescence in $Ba_{1+x}La_{4-x}Si_3O_{13-x/2}$:Eu ($x \sim 1.5$). The successful reduction of Eu^{3+} to Eu^{2+} in $Ba_{1+x}La_{4-x}Si_3O_{13-x/2}$ (from $x = 0$ to $x \sim 1.5$) is further confirmed by the high-resolution X-ray photoelectron spectroscopy (XPS) spectrum of the Eu 3d orbitals (Figure 6a). The binding energy peaking at ~1136 eV is ascribed to the Eu^{3+} ions, while the peak at ~1128 eV is ascribed to the Eu^{2+} ions in $Ba_{1+x}La_{4-x}Si_3O_{13-x/2}$. The apparent decrease in the Eu^{3+} binding energy peak intensity in $Ba_{1+x}La_{4-x}Si_3O_{13-x/2}$ ($x \sim 1.5$) confirms the successful reduction of Eu^{3+} with an excess of M. As stated earlier, based on the principle of charge neutrality, the insertion of M cations in $M_{1+x}La_{4-x}Si_3O_{13-x/2}$ would simultaneously introduce oxygen vacancies ($V_O^{\bullet\bullet}$). The gradual insertion of the M cations and formation of $V_O^{\bullet\bullet}$ result in a continuous change of the host's structural and electronic properties, which affects the PL of the *in-crystal* Eu^{2+}. The ^{29}Si NMR spectrum (Figure 6b) shows a slightly blue-shifted sharp signal centered at −77 ppm at $Ba_{1+x}La_{4-x}Si_3O_{13-x/2}$:Eu ($x \sim 1.5$) compared to the composition at $x = 0$ (−83 ppm), which is attributed to the expansion of the $[SiO_4]$ polyhedron. The preserved shape of the Si NMR spectrum suggests that the $V_O^{\bullet\bullet}$ is primarily formed

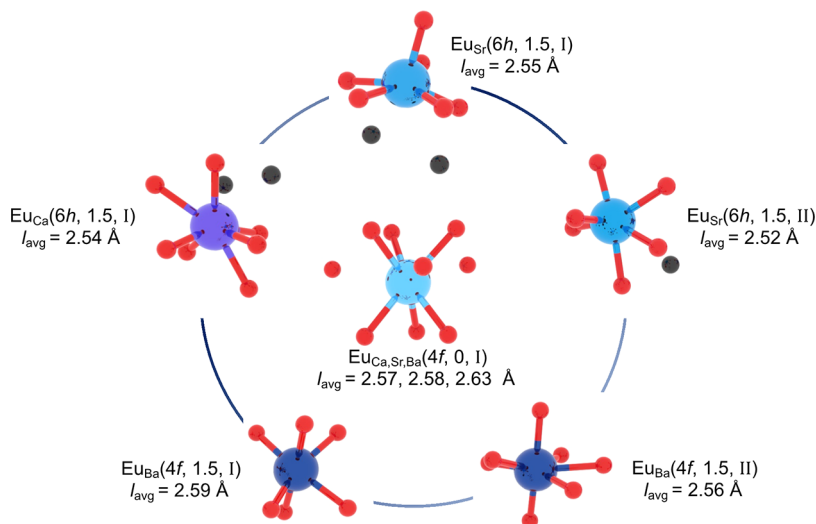**Figure 7.** Local environment evolution of Eu^{2+} in the apatite $M_{1+x}La_{4-x}Si_3O_{13-x/2}$ from $x = 0$ to $x = 1.5$. The central blue spheres refer to Eu^{2+}, the red spheres denote the oxygen ligands, and the black spheres refer to the oxygen vacancies. The general notation of $Eu_M(Wy, x, \omega)$ is used to denote the Wyckoff position (Wy) of the Eu^{2+} polyhedron in the apatite composition with M cations of the x concentration, and ω stands for the two lowest-energy $Eu^{2+}-V_O^{\bullet\bullet}$ configurations in the given compositions.

around the main cations (M and La) and raises the importance of determining the Eu^{2+} local environment for understanding PL behaviors of the phosphor compositions. The structural distributions of Eu^{2+} and $V_O^{\bullet\bullet}$ will be investigated in detail in the next section by DFT calculations.

Computational Structural and Chemical Analysis of PL Behaviors. The determination of Eu^{2+} site preference in the experiment is challenging because of the very low activator concentrations. Alternatively, we performed DFT calculations on $Eu^{2+/3+}$-activated $MLa_4Si_3O_{13}$ and evaluated charge-neutral defect formation energies (ΔE_f^d) of Eu^{2+} on M^{2+} and Eu^{3+} on La^{3+}. The calculated ΔE_f^d values are shown in Table 3. It is found that ΔE_f^d of Eu_M ($\Delta E_f^d = 0.06, 0.10$, and -0.21 eV/Eu for Eu_{Ca}, Eu_{Sr}, and Eu_{Ba}, respectively) is lower than that of Eu_{La} ($\Delta E_f^d > 2.24$ eV/Eu), suggesting that Eu^{2+} primarily occupies the M_{4f} sites. Moreover, ΔE_f^d of Eu_{La} in $LaSiO_2N$ is 1.91 (4f site) and 2.12 (6h site) eV/Eu, which is smaller than that of Eu_{La} in $MLa_4Si_3O_{13}$:Eu. These results suggest that the PL spectra of $MLa_4Si_3O_{13}$:Eu would predominantly show a broadband emission from Eu^{2+} and a limited emission from Eu^{3+}. As shown in Figure 5a–c, the emission spectra of $MLa_4Si_3O_{13}$:Eu exhibit a much lower intensity of the Eu^{3+} characteristic peak compared to those of $LaSiO_2N$:Eu, following the calculated trend from ΔE_f^d of Eu_{La} in $MLa_4Si_3O_{13}$:Eu (Table 3) and confirming the stabilization of Eu^{2+} in the M_{4f} sites.

We performed DFT calculations on Eu^{2+}/Eu^{3+}-activated $LaSiO_2N$ and $M_{1+x}La_{4-x}Si_3O_{13-x/2}$ ($x = 0$ and 1.5) and evaluated charge-neutral defect formation energies (ΔE_f^d) of Eu^{2+}/Eu^{3+} on M^{2+}/La^{3+}. For brevity, the general notation of $\Delta E_f^d[Eu_{La}, Wy]$ and $\Delta E_f^d[Eu_M, Wy]$ is used to denote the dopant formation energies of substituting La^{3+} by Eu^{3+} and M^{2+} by Eu^{2+}, respectively, and the site Wyckoff position (Wy). The computed ΔE_f^d values are shown in Table 3. At $x = 0$ in $M_{1+x}La_{4-x}Si_3O_{13-x/2}$, the computed $\Delta E_f^d[Eu_M, Wy]$ suggests that Eu^{2+} activators are stabilized at the M_{4f} sites, that is, $\Delta E_f^d[Eu_M, 4f] = 0.06, 0.10$, and -0.213 eV/Eu^{2+} for $M = Ca/Sr$ and Ba at $x = 0$, while $\Delta E_f^d[Eu_{La}, Wy]$ is considerably higher ($\Delta E_f^d[Eu_{La}, Wy] > 2.2$ eV/Eu^{3+}). Moreover, it is noted that $\Delta E_f^d[Eu_{La}, 4d/8f]$ in $LaSiO_2N$ are relatively higher than those

in $MLa_4Si_3O_{13}$. These results confirm our initial hypothesis of the increased stability of Eu^{2+} upon the M insertion in the $LaSiO_2N$ lattice and explain the observed broadband emission from Eu^{2+} in $MLa_4Si_3O_{13}$:Eu and the reduced characteristic emission of Eu^{3+} (Figure 5). The energy difference between $\Delta E_f^d[Eu_{La}, Wy]$ and $\Delta E_f^d[Eu_M, Wy]$ in $MLa_4Si_3O_{13}$ (Table 3) increases from $M = Ca$ to $M = Ba$ and is correlated to the amount of characteristic Eu^{3+} emission present in the PL spectra (Figure 5a–c).

The continuous insertion of M cations in $M_{1+x}La_{4-x}Si_3O_{13-x/2}$ ($x = 1.5$) leads to the formation of oxygen vacancies, which should occur in the close vicinity of M and La^{3+} cations according to the ^{29}Si NMR spectrum measurements. The formation of such vacancies will result in a decreased lattice symmetry and the formation of distinct M/La local environments. Accordingly, we have considered the insertion of Eu^{2+} and Eu^{3+} in all available M/La crystallographic sites. Figure S9 shows the computed site energies for Eu^{2+} substituting M cations in $M_{1+x}La_{4-x}Si_3O_{13-x/2}$ at $x = 1.5$. For $M = Sr$ and Ba, the site energy difference between the two lowest Eu^{2+} configurations is lower than 25 meV/Eu^{2+}, suggesting that the Eu^{2+}-activated apatite possesses two distinct luminescent centers, in line with the observed dual-peak emission (Figure 5a–d). For $Ca_{1+x}La_{4-x}Si_3O_{13-x/2}$:Eu^{2+}, however, the site energy difference between the two lowest Eu^{2+} configurations is 254 meV/Eu^{2+}, suggesting the presence of a single emission peak, as confirmed by the measured emission spectrum of $Ca_{1+x}La_{4-x}Si_3O_{13-x/2}$:Eu^{2+} (Figure 5a). Finally, it is noted that the computed $\Delta E_f^d[Eu_{La}, Wy]$ in $M_{1+x}La_{4-x}Si_3O_{13-x/2}$ ($x = 1.5$) are considerable higher than $\Delta E_f^d[Eu_M, Wy]$, confirming the stabilization of Eu^{2+} in the M sites (Table 3).

To understand the spectral evolution with respect to x in the Eu^{2+}-activated $M_{1+x}La_{4-x}Si_3O_{13-x/2}$ hosts, we analyzed the $Eu^{2+}-V_O^{\bullet\bullet}$ structural distributions obtained from the DFT-optimized $M_{1+x}La_{4-x}Si_3O_{13-x/2}$:Eu^{2+} ($x = 0$ and 1.5) models. We examine the impact of oxygen vacancies on the Eu^{2+} polyhedrons. The general notation of $Eu_M(Wy, x, \omega)$ is used to characterize the Eu^{2+} polyhedrons in the apatite structure, where the Wyckoff position is denoted by Wy, x defines the

M/La/O concentrations in $M_{1+x}La_{4-x}Si_3O_{13-x/2}$, and ω stands for the two lowest-energy $Eu^{2+}-V_O^{\bullet\bullet}$ configurations in the given composition. Here, ω has two possible values labeled by the roman numeral I or II, where I refers to the lowest-energy configuration. The spatial distribution of $Eu^{2+}-V_O^{\bullet\bullet}$ differs from one composition to another and is classified into two distinct categories: (i) $V_O^{\bullet\bullet}$ located within the first-shell environment of Eu^{2+} and (ii) $V_O^{\bullet\bullet}$ located beyond the first-shell environment of Eu^{2+}. For $Eu_{Sr/Ca}(6h, 1.5, I/II)$, as shown in Figure S10, oxygen vacancies adopt scenario (i), while for $Eu_{Ba}(4f, 1.5, I/II)$, the oxygen vacancies adopt scenario (ii). Precisely, the initial trigonal prism with an average bond length (l_{avg}) of 2.59 Å at $Eu_{Ba}(4f, 0, I)$ transforms to an octahedron (Oct) shape with reduced bond lengths (Oct; l_{avg} = 2.56 Å) at $Eu_{Ba}(4f, 1.5, I)$, while seven oxygen ligands are present around $Eu_{Ba}(4f, 1.5, II)$ forming a pentagonal bipyramidal polyhedron (l_{avg} = 2.59 Å). The synergetic combination of the polyhedron size reduction and shape alteration (TP to Oct) at $Eu_{Ba}(4f, 1.5, I)$ is expected to induce a longer emission wavelength, and consequently, $Eu_{Ba}(4f, 1.5, I)$ is assigned to the experimentally measured λ_{em} peak at 635 nm (Figure 5). In contrast, $Eu_{Ba}(4f, 1.5, II)$ is matched with the λ_{em} peak at 510 nm. For $Sr_{1+x}La_{4-x}Si_3O_{13-x/2}$:$Eu^{2+}$, $V_O^{\bullet\bullet}$ is formed around the first-shell environment (scenario i) of both $Eu_{Sr}(6h, 1.5, I)$ and $Eu_{Sr}(6h, 1.5, II)$ transforming the initial TP (l_{avg} = 2.60 Å) to a pentagonal pyramid (PP: 6), with respective l_{avg} values of 2.55 and 2.52 Å (Figure S10, Table S4). These local environment alterations are predicted to induce two red-shifted emission peaks. Finally, $V_O^{\bullet\bullet}$ adopts scenario (i) for $Eu_{Ca}(6h, 1.5, I)$, reducing the polyhedron size from (l_{avg} = 2.60 Å) at $Eu_{Ca}(4f, 0, I)$ to 2.54 Å for $Eu_{Ca}(6h, 1.5, I)$ (Figure S10, Table S4). The presence of a single reduced polyhedron is expected to induce a single, red-shifted emission peak at x = 1.5. These geometry evolutions are summarized in Figure 7 for each studied composition. The PL and activator's polyhedron geometrical property evolution from x = 0 to x = 1.5 are also summarized in Table 4. Finally, it is noted that for both M = Ca and Sr at x = 1.5, oxygen vacancies in the first-shell environment of Eu^{2+} are most likely capable of partially oxidizing some of the Eu^{2+} activators and consequently explaining the negligible characteristic emission from Eu^{3+}. In contrast, for M = Ba, no traces of Eu^{3+} emission are observed, coinciding with the absence of oxygen vacancies within the first-shell environment of Eu^{2+}.

Thermal Quenching Mechanism. The thermal quenching (TQ) behavior of $M_{1+x}La_{4-x}Si_3O_{13-x/2}$:Eu was further investigated. As shown in Figures 8 and S11, the composition at x = 1.5 shows a significant improvement of thermal stability compared to that at x = 0. In particular, the thermal stability of $Ba_{1+x}La_{4-x}Si_3O_{13-x/2}$:Eu (Figure 8a) is 82% at 573 K, whereas $LaSiO_2N$:Eu only maintains 19% of its room temperature intensity at 573 K. Compared to x = 0, the thermal stability of $M_{1+x}La_{4-x}Si_3O_{13-x/2}$:Eu ($x$ = 1.5) is also significantly enhanced for M = Ba and Sr, while the Ca-type is only slightly enhanced (Table 4). Here, we use the dual-energy barrier model[16] to interpret the TQ change from x = 0 to 1.5 in $M_{1+x}La_{4-x}Si_3O_{13-x/2}$:Eu. In the dual-energy barrier model, two key parameters synergistically control TQ: namely, the auto-ionization energy barrier (E_a^i) and the activator's local environment rigidity. As mentioned earlier, the gradual insertion of M cations in $M_{1+x}La_{4-x}Si_3O_{13-x/2}$ leads to a red-shifted emission in all cases. Consequently, lowering the relaxed, excited 5d state induces a larger E_a^i and reduces the auto-ionization quenching. On the other hand, the red-shifted

Table 4. PL and Eu^{2+} Polyhedron Evolution in $M_{1+x}La_{4-x}Si_3O_{13-x/2}$ (x = 0 and 1.5, M = Ca/Sr/Ba) Compounds[a]

polyhedron	geometry	l_{avg} (Å)	λ_{em} (nm)	γ %	TS %
$Eu_{Ca}(6h, 0, I)$	TP	2.57	517	47	48
$Eu_{Ca}(6h, 1.5, I)$	PTP	2.54	546	53	52
$Eu_{Sr}(4f, 0, I)$	TP	2.58	510	47	47
$Eu_{Sr}(6h, 1.5, II)$	PP	2.55	536	71	80
$Eu_{Sr}(6h, 1.5, II)$	PP	2.52	564		
$Eu_{Ba}(4f, 0, I)$	TP	2.63	503	47	50
$Eu_{Ba}(4f, 1.5, I)$	PB	2.59	510	77	87
$Eu_{Ba}(4f, 1.5, II)$	Oct	2.56	635		

[a]The general notation of $Eu_M(Wy, x, \omega)$ is used to denote the Wyckoff position (Wy) of the Eu^{2+} polyhedron in the apatite composition with the x M concentration, and ω stands for the two lowest-energy $Eu^{2+}-V_O^{\bullet\bullet}$ configurations in the given compositions. The geometry of the Eu^{2+} polyhedron is denoted by the following: TP for trigonal prism, PTP for pentagonal trigonal prism, PP for pentagonal prism, and PB for pentagonal bi-pyramidal. l_{avg} is the average bond length of the polyhedron in angstrom (Å). λ_{em} is the experimentally measured emission wavelength in nanometer (nm). γ is the Eu^{2+} polyhedron Voronoi area given in percent area. TS stands for the measured thermal stability and is determined by taking the ratio of the integrated light intensity emitted at 500 K and the integrated intensity emitted of the light emitted at room temperature (300 K).

emission is caused by dramatic geometrical changes around Eu^{2+}. These geometrical changes are thus investigated in terms of their local environment rigidity via the Voronoi grid representation. For $Eu_{Ba}(4f, 0, I)$, the Voronoi grid representation (Figure 8b,c) primarily forms a sixfold and ninefold environment with an effective coordination number (ECoN) of 7.1; while for $Eu_{Ba}(4f, 1.5, I)$, Eu^{2+} is displaced from the center of the trigonal prism to form an octahedron geometry (CN = 6) with an ECoN of 6.4. Accordingly, the Voronoi area (Y) around the ECoNs increases (by 30%) from 47% at $Eu_{Ba}(4f, 0, I)$ to 77% at $Eu_{Ba}(4f, 1.5, I)$. Similarly, the ECoN around $Eu_{Sr}(4f, 0, I)$ and $Eu_{Sr}(6h, 1.5, I)$ is 7.25 and 5.5, respectively, resulting in respective Y values of 47 and 71% (24% increase) (Figure S11b). The increase in Y reflects an increase in the local environment rigidity at $Eu_{Ba}(4f, 1.5, I)$ and $Eu_{Sr}(6h, 1.5, I)$ compared to $Eu_{Ba}(4f, 0, I)$ and $Eu_{Sr}(4f, 0, I)$, which explains the enhanced thermal stability of $Ba_{1+x}La_{4-x}Si_3O_{13-x/2}$:$Eu^{2+}$ and $Sr_{1+x}La_{4-x}Si_3O_{13-x/2}$:$Eu^{2+}$. Finally, the ECoN around $Eu_{Ca}(4f, 0, I)$ and $Eu_{Ca}(6h, 1.5, I)$ is 7.22 and 6.2, respectively, with respective Y values of 47 and 53% (6% increase) (Figure S11e,f). The small increase in Y is thus reflected by the relatively smaller enhancement of thermal stability for $Ca_{1+x}La_{4-x}Si_3O_{13-x/2}$:Eu. The super broadband emission with a bandwidth of ~290 nm, excellent thermal stability, and improved QE (Table S5) enables potential white LEDs with high power and color quality. A white LED device was fabricated (Figure 9a) with the commercial blue phosphor BAM:Eu and broadband phosphor $Ba_{1+x}La_{4-x}Si_3O_{13-x/2}$:Eu on a UV LED chip ($\lambda_{em}$ = 365 nm). Under a high driven current of 500 mA, a standard white light was created with chromaticity coordinates located at 0.32 and 0.33, a CRI of 93, and a CCT of 6080 K (Figure 9b).

CONCLUSIONS

In summary, we have thoroughly investigated the luminescence properties of $LaSiO_2N$:Eu^{2+} and $M_{1+x}La_{4-x}Si_3O_{13-x/2}$. By
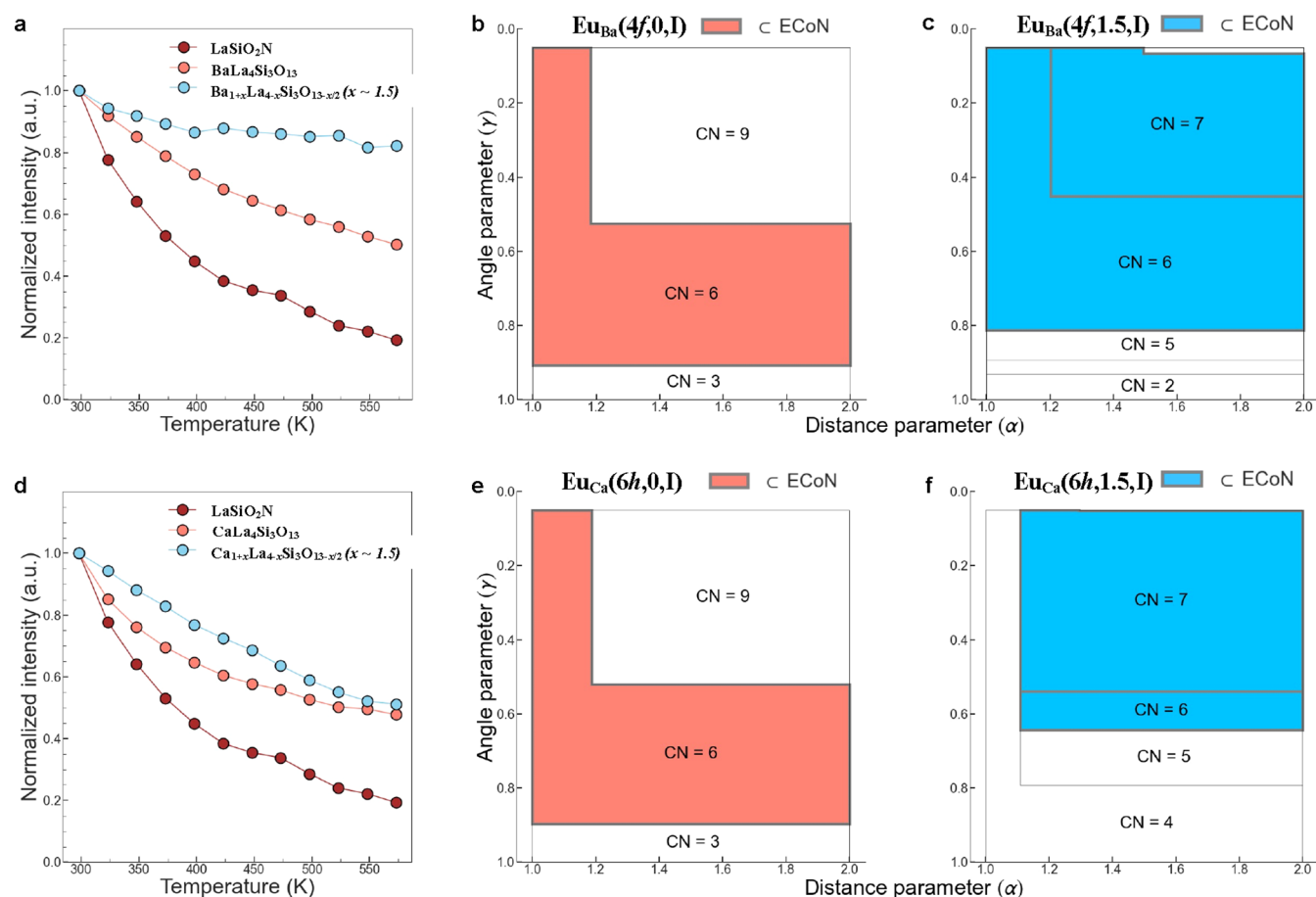
Figure 8. TQ behaviors of Eu-activated $M_{1+x}La_{4-x}Si_3O_{13-x/2}$:Eu ($M$ = Ca/Sr/Ba) compounds and the activator's local structure rigidity. (a) Experimental TQ of LaSiO$_2$N:Eu$^{3+/2+}$, BaLa$_4$Si$_3$O$_{13}$:Eu^{2+}, and Ba$_{1+x}$La$_{4-x}$Si$_3$O$_{13-x/2}$:Eu^{2+}. (b,c) Graphical depictions of the two-dimensional reduction presented by the Voronoi grid representation of Eu^{2+} in BaLa$_4$Si$_3$O$_{13}$ and Ba$_{1+x}$La$_{4-x}$Si$_3$O$_{13-x/2}$. (d) Experimental TQ of LaSiO$_2$N:Eu$^{3+/2+}$, CaLa$_4$Si$_3$O$_{13}$:Eu^{2+}, and Ca$_{1+x}$La$_{4-x}$Si$_3$O$_{13-x/2}$:Eu^{2+}. (e,f) Graphical depictions of the two-dimensional reduction presented by the Voronoi grid representation of Eu^{2+} in CaLa$_4$Si$_3$O$_{13}$ and Ca$_{1+x}$La$_{4-x}$Si$_3$O$_{13-x/2}$.

combining DFT-based crystal structure predictions and advanced experimental characterizations (SXRD, SAED, and NMR), we have resolved the crystal structure of LaSiO$_2$N with the monoclinic $C2/c$ (no. 15) phase and determined the La local coordination. The reduction of the undesired emission of Eu^{3+} and the luminescence improvement of LaSiO$_2$N:Eu were strategically conducted by engineering the luminescent active sites' thermodynamics stability and polyhedral geometries *via* divalent-cation substitutions. The developed $M_{1+x}La_{4-x}Si_3O_{13-x/2}$:Eu^{2+} ($x$ = 1.5, M = Ca/Sr/Ba) apatite phases showcase a super-broad emission, enhanced QE, and excellent thermal stability. A detailed investigation of the impact of the hosts−Eu interactions sheds light on the luminescence evolution as a response to divalent-cation substitutions and reveals the crucial and previously concealed importance of oxygen defects to alter and improve phosphors' luminescent properties drastically.

◼ MATERIALS AND METHODS

Computational Methods. All DFT calculations were performed using the Vienna *ab initio* simulation package within the projected-augmented wave method.[17,18] The exchange−correlation was treated using the Perdew−Burke−Ernzerhof generalized gradient approximation functional.[19] The plane-wave energy cutoff was 520 eV. The electronic energy and force were converged to 10^{-5} eV and 0.01 eV/Å, respectively. The Brillouin zone was calculated with a k-point grid

of at least 100 per Å^{-3}. For host structure calculations, we used the parameters in line with the Materials Project.[20] For Eu-doped hosts, we used a Hubbard U value of 2.5 eV for Eu 4f.[21] All structure manipulation and data analysis were carried out using the Python Materials Genomics (pymatgen) package.[22]

The phonon spectrum of LaSiO$_2$N was calculated using the finite difference method as implemented in the Phonopy code.[23] More stringent energy and force criteria of 10^{-8} eV and 10^{-4} eV/Å were used in this calculation. The Gibbs free energy was calculated at constant volume under quasi-harmonic approximation. The pressure was evaluated by fitting the $E-V$ curve using the Murnaghan equation of state. The enthalpy change was then calculated with $\Delta H = \Delta E + p\Delta V$ by assuming that the entropy difference between solids is very small. The solid phase transformation barrier was calculated using the VC-NEB method.[14]

Using the algorithm of Waroquiers *et al.*[24] as implemented in the pymatgen package, the local environments were computed. The notion of Hoppe's effective coordination number (ECoN)[15] determined the bond weights between cation and oxygen ligands based on the polyhedral geometry. The Voronoi grid representation was computed using two variables, namely, the maximum distance factor and the angular parameter. The combination of both parameters defines a unique set of ligands forming a polyhedron.

Sample Preparation. The non-doped and Eu-doped LaSiO$_2$N, MLa$_4$Si$_3$O$_{13}$, and M_{1+x}La$_{4-x}$Si$_3$O$_{13-x/2}$ ($x \sim 1.5$) (M = Ca/Sr/Ba) powders were prepared by firing the raw mixture of La$_2$O$_3$, SiO$_2$, Si$_3$N$_4$, MCO$_3$ (M = Ca/Sr/Ba), and/or Eu$_2$O$_3$ according to the stoichiometric compositions. The sintering process of LaSiO$_2$N was
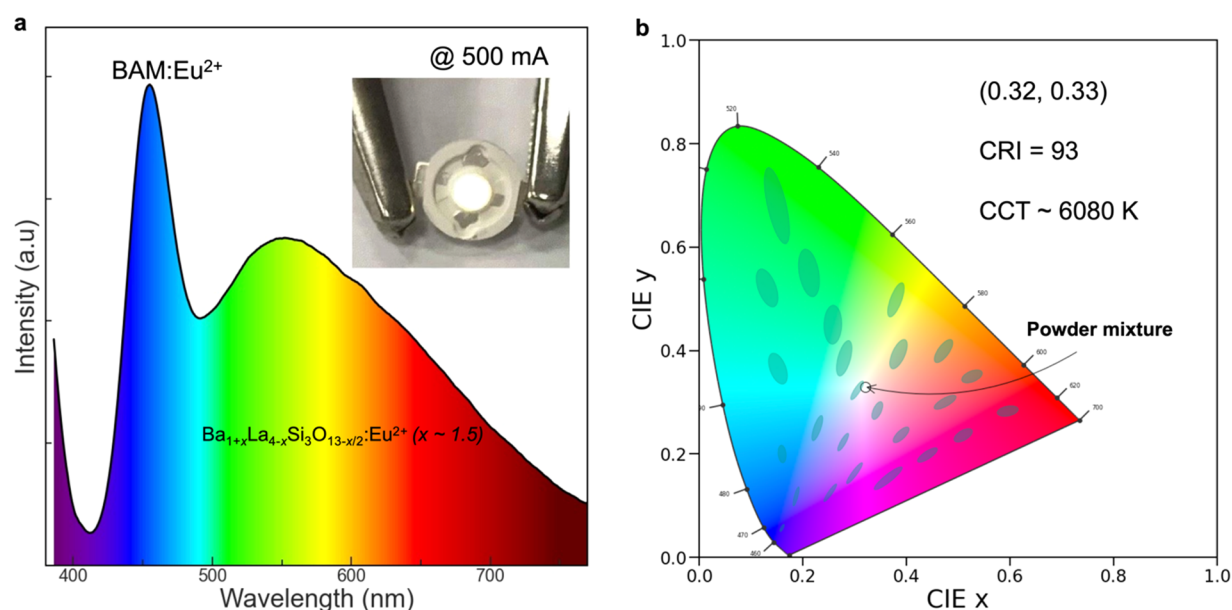
Figure 9. Performance of the white phosphor-converted LED device. (a) Electroluminescence spectrum of the white LED device fabricated with the commercial blue phosphor BAM:Eu and broadband $Ba_{1+x}La_{4-x}Si_3O_{13-x/2}$:Eu on a UV LED chip ($\lambda_{em}$ = 365 nm) under a current of 500 mA, and the inset is the photograph of the fabricated white LED. (b) Plot of the CIE coordinate of the powder mixture of BAM:Eu^{2+} and $Ba_{1+x}La_{4-x}Si_3O_{13-x/2}$:Eu^{2+} phosphors under an excitation of 365 nm. The CIE diagram is decorated with MacAdam ellipses and defines regions where the colors are indistinguishable for the human eye.

conducted in a gas pressure sintering furnace (Shimadzu, Kyoto, Japan) at 1600−1700 °C for 4 h under a nitrogen pressure of 0.9 MPa. The synthesis of MLa$_4$Si$_3$O$_{13}$ and M_{1+x}La$_{4-x}$Si$_3$O$_{13-x/2}$ (x = 1.5) was carried out in a horizontal tube furnace at 1300−1500 °C for 6 h under a flowing N$_2$−10% H$_2$. After cooling, they were finely ground for characterizations.

Sample Characterizations. The SXRD pattern was collected at the BL01C2 beamline of the National Synchrotron Radiation Research Center (Taiwan) at a wavelength of 0.82657 Å. Total pattern analysis solution software was used to perform XRD Rietveld refinement. The ordinary XRD patterns were collected by using a powder X-ray diffractometer (D8 Advance, Bruker, Germany). The cationic elements were measured with inductively coupled plasma atomic emission spectrometry (Vista AX, Varian, USA). The TEM and STEM analyses were conducted using a JEM-2100F electron microscope (JEOL, Japan) equipped with CL and EDS attachments. The solid-state ^{29}Si NMR experiment was performed on an NMR 400 MHz spectrometer (Bruker AVANCE III, Switzerland) at room temperature. XPS was conducted on a Thermo Scientific K-Alpha spectrometer equipped with a monochromatic Al Kα X-ray source (1486.6 eV) operating at 100 W. The PL spectra were measured with a steady-state fluorescence spectrometer (FLS980, Edinburgh Instruments Ltd., UK). The QE was measured with an absolute PL quantum yield spectrometer (Quantaurus-QY, Hamamatsu Photonics, Tokyo, Japan). The thermal stability was measured with a homemade measurement system consisting of a 365 nm LED light source, a cooling/heating stage (THMS600E, Linkam Scientific Instruments, UK), and a CCD spectrometer (USB2000+, Ocean Optics, USA). The thermoluminescence curves were recorded *via* a homemade measurement system which is driven by LabVIEW-based PC programs. The performance of the white LED was evaluated by using an auto-temperature LED optoelectronic analyzer (ATA-500, Everfine Co., Hangzhou, China) under a bias current of 500 mA.

ASSOCIATED CONTENT

Supporting Information

The Supporting Information is available free of charge at https://pubs.acs.org/doi/10.1021/acs.chemmater.2c00252.

Isothermal section of the Si$_3$N$_4$−SiO$_2$−La$_2$O$_3$ system at 1700 °C, calculated Gibbs and enthalpy energy difference between $C2/c$ and $P6_122$ for LaSiO$_2$N, XRD patterns of different LaSiO$_2$N phases both reported in the literature and predicted in this work, crystal structures of LaSiO$_2$N with the space group of $P\bar{6}c2$ in the literature, Wyckoff positions of oxygen anions in MLa$_4$Si$_3$O$_{13}$, XRD Rietveld refinements of M_{1+x}La$_{4-x}$Si$_3$O$_{13-x/2}$ ($x \sim 1.5$), chemical characterizations of M_{1+x}La$_{4-x}$Si$_3$O$_{13-x/2}$ ($x \sim 1.5$), computed prototypal structure of MLa$_4$Si$_3$O$_{13}$ and M_{1+x}La$_{4-x}$Si$_3$O$_{13-x/2}$, site energies of Eu in M_{1+x}La$_{4-x}$Si$_3$O$_{13-x/2}$, DFT-optimized M_{1+x}La$_{4-x}$Si$_3$O$_{13-x/2}$:Eu^{2+} supercells and the spatial distribution of Eu^{2+}−V$_O^{\bullet\bullet}$, comparison of the TQ behavior and the Voronoi grid areas between LaSiO$_2$N:Eu, SrLa$_4$Si$_3$O$_{13}$:Eu^{2+}, and Sr$_{1+x}$La$_{4-x}$Si$_3$O$_{13-x/2}$:Eu^{2+}, atomic site occupancy of LaSiO$_2$N with space group $P6_122$, bond length of La−O/N for the $C2/c$ phase of LaSiO$_2$N, structural parameters of LaSiO$_2$N ($C2/c$) and promising MLa$_4$Si$_3$O$_{13}$ structures, element contents in as-prepared M_{1+x}La$_{4-x}$Si$_3$O$_{13-x/2}$ ($x \sim 1.5$) compounds, and quantum efficiency and absorption efficiency in Eu-activated MLa$_4$Si$_3$O$_{13}$ and M_{1+x}La$_{4-x}$Si$_3$O$_{13-x/2}$ ($x \sim 1.5$) compounds (PDF)

AUTHOR INFORMATION

Corresponding Authors

Zhenbin Wang − *Department of Nanoengineering, University of California San Diego, La Jolla, California 92093-0448, United States;* orcid.org/0000-0002-7016-9245; Email: z9wang@eng.ucsd.edu

Rong-Jun Xie − *College of Materials, Xiamen University, Xiamen 361005, China;* orcid.org/0000-0002-8387-1316; Email: rjxie@xmu.edu.cn

Shyue Ping Ong − *Department of Nanoengineering, University of California San Diego, La Jolla, California 92093-0448, United States;* ⊙ orcid.org/0000-0001-5726-2587; Email: ongsp@eng.ucsd.edu

Authors

Mahdi Amachraa − *Department of Nanoengineering, University of California San Diego, La Jolla, California 92093-0448, United States;* ⊙ orcid.org/0000-0003-3001-3630

Shuxing Li − *College of Materials, Xiamen University, Xiamen 361005, China;* ⊙ orcid.org/0000-0001-8086-7154

Po-Yuan Huang − *Department of Chemistry, National Taiwan University, Taipei 106, Taiwan*

Ru-Shi Liu − *Department of Chemistry, National Taiwan University, Taipei 106, Taiwan;* ⊙ orcid.org/0000-0002-1291-9052

Complete contact information is available at:
https://pubs.acs.org/10.1021/acs.chemmater.2c00252

Author Contributions

M.A. and S.L. contributed equally to this work. S.P.O. and R.-J.X. supervised the project. M.A. and Z.W. performed the DFT calculations, analyzed the data, and prepared the article. S.L. conducted the experiments and analyzed the data. P.-Y.H. and R.-S.L. measured and analyzed the SXRD patterns. All authors contributed to the discussions and revisions of the article.

Notes

The authors declare no competing financial interest.

■ REFERENCES

(1) Shea, J. J. Handbook of Optical Materials [Book Review]. *IEEE Electr. Insul. Mag.* **2004**, *20*, 46.

(2) Judd, B. R. Correlation Crystal Fields for Lanthanide Ions. *Phys. Rev. Lett.* **1977**, *39*, 242−244.

(3) Dorenbos, P. Relation between Eu^{2+} and Ce^{3+} f↔d-Transition energies in inorganic compounds. *J. Phys.: Condens. Matter* **2003**, *15*, 4797−4807.

(4) Huang, X.; Qiao, Z.; Qiu, Z.; Ma, N.; Wen, J.; Ning, L. Site Occupation and Spectral Assignment in Eu^{2+}-Activated β-Ca$_3$(PO$_4$)$_2$-Type Phosphors: Insights from First-Principles Calculations. *Inorg. Chem.* **2020**, *59*, 16760−16768.

(5) Qin, X.; Liu, X.; Huang, W.; Bettinelli, M.; Liu, X. Lanthanide-Activated Phosphors Based on 4f-5d Optical Transitions: Theoretical and Experimental Aspects. *Chem. Rev.* **2017**, *117*, 4488−4527.

(6) Wang, L.; Xie, R.-J.; Suehiro, T.; Takeda, T.; Hirosaki, N. Down-Conversion Nitride Materials for Solid State Lighting: Recent Advances and Perspectives. *Chem. Rev.* **2018**, *118*, 1951−2009.

(7) Xia, Z.; Liu, Q. Progress in Discovery and Structural Design of Color Conversion Phosphors for LEDs. *Prog. Mater. Sci.* **2016**, *84*, 59−117.

(8) Mitomo, M.; Izumi, F.; Horiuchi, S.; Matsui, Y. Phase Relationships in the System Si$_3$N$_4$-SiO$_2$-La$_2$O$_3$. *J. Mater. Sci.* **1982**, *17*, 2359−2364.

(9) Wills, R. R.; Cunningham, J. A. Silicon Cerium Oxynitride. *J. Mater. Sci.* **1977**, *12*, 208−210.

(10) Morgan, P. E. D.; Carroll, P. J. The Crystal Structures of CeSiO$_2$N and LaSiO$_2$N. *J. Mater. Sci.* **1977**, *12*, 2343−2344.

(11) Hautier, G.; Fischer, C.; Ehrlacher, V.; Jain, A.; Ceder, G. Data Mined Ionic Substitutions for the Discovery of New Compounds. *Inorg. Chem.* **2011**, *50*, 656−663.

(12) Bergerhoff, G.; Hundt, R.; Sievers, R.; Brown, I. D. The Inorganic Crystal Structure Data Base. *J. Chem. Inf. Comput. Sci.* **1983**, *23*, 66−69.

(13) Wenk, H. -R. Polymorphism of Wollastonite. *Contrib. to Mineral. Petrol.* **1969**, *22*, 238−247.

(14) Qian, G.-R.; Dong, X.; Zhou, X.-F.; Tian, Y.; Oganov, A. R.; Wang, H.-T. Variable Cell Nudged Elastic Band Method for Studying Solid-Solid Structural Phase Transitions. *Comput. Phys. Commun.* **2013**, *184*, 2111−2118.

(15) Hoppe, R. The Coordination Number—an "Inorganic Chameleon". *Angew. Chem., Int. Ed.* **1970**, *9*, 25−34.

(16) Amachraa, M.; Wang, Z.; Chen, C.; Hariyani, S.; Tang, H.; Brgoch, J.; Ong, S. P. Predicting Thermal Quenching in Inorganic Phosphors. *Chem. Mater.* **2020**, *32*, 6256−6265.

(17) Kresse, G.; Furthmüller, J. Efficient Iterative Schemes for *Ab Initio* Total-Energy Calculations Using a Plane-Wave Basis Set. *Phys. Rev. B: Condens. Matter Mater. Phys.* **1996**, *54*, 11169−11186.

(18) Blöchl, P. E. Projector Augmented-Wave Method. *Phys. Rev. B: Condens. Matter Mater. Phys.* **1994**, *50*, 17953−17979.

(19) Perdew, J. P.; Burke, K.; Ernzerhof, M. Generalized Gradient Approximation Made Simple. *Phys. Rev. Lett.* **1996**, *77*, 3865−3868.

(20) Jain, A.; Ong, S. P.; Hautier, G.; Chen, W.; Richards, W. D.; Dacek, S.; Cholia, S.; Gunter, D.; Skinner, D.; Ceder, G.; Persson, K. A. Commentary: The Materials Project: A Materials Genome Approach to Accelerating Materials Innovation. *APL Mater.* **2013**, *1*, 011002.

(21) Chaudhry, A.; Boutchko, R.; Chourou, S.; Zhang, G.; Grønbech-Jensen, N.; Canning, A. First-Principles Study of Luminescence in Eu^{2+}-Doped Inorganic Scintillators. *Phys. Rev. B: Condens. Matter Mater. Phys.* **2014**, *89*, 155105.

(22) Ong, S. P.; Richards, W. D.; Jain, A.; Hautier, G.; Kocher, M.; Cholia, S.; Gunter, D.; Chevrier, V. L.; Persson, K. A.; Ceder, G. Python Materials Genomics (Pymatgen): A Robust, Open-Source Python Library for Materials Analysis. *Comput. Mater. Sci.* **2013**, *68*, 314−319.

(23) Togo, A.; Tanaka, I. First principles phonon calculations in materials science. *Scr. Mater.* **2015**, *108*, 1−5.

(24) Waroquiers, D.; Gonze, X.; Rignanese, G.-M.; Welker-Nieuwoudt, C.; Rosowski, F.; Göbel, M.; Schenk, S.; Degelmann, P.; André, R.; Glaum, R.; Hautier, G. Statistical Analysis of Coordination Environments in Oxides. *Chem. Mater.* **2017**, *29*, 8346−8360.